Title

Fermi level tuning and double-dome superconductivity in the kagome metal $CsV_3Sb_{5-x}Sn_x$

Journal

Physical Review Materials, 6(4)

ISSN

2475-9953

Authors

Oey, Yuzki M
Ortiz, Brenden R
Kaboudvand, Farnaz
et al.

Publication Date

2022-04-06

DOI

10.1103/PhysRevMaterials.6.L041801

Peer reviewed

Fermi level tuning and double-dome superconductivity in the kagome metal $CsV_3Sb_{5-x}Sn_x$

Yuzki M. Oey,[1] Brenden R. Ortiz,[1] Farnaz Kaboudvand,[1] Jonathan Frassineti,[2,3] Erick Garcia,[2] Rong Cong,[2] Samuele Sanna,[3] Vesna F. Mitrović,[2] Ram Seshadri,[1] and Stephen D. Wilson[1]

[1]*Materials Department, Materials Research Laboratory, and California NanoSystems Institute University of California Santa Barbara, California 93106 United States**

[2]*Department of Physics, Brown University, Providence, RI 02912, U.S.A.*

[3]*Department of Physics and Astronomy "A. Righi", University of Bologna, I-40127 Bologna, Italy*

(Dated: April 6, 2022)

The recently reported AV_3Sb_5 (A = K, Rb, Cs) family of kagome metals are candidates for unconventional superconductivity and chiral charge density wave (CDW) order; both potentially arise from nested saddle points in their band structures close to the Fermi energy. Here we use chemical substitution to introduce holes into CsV_3Sb_5 and unveil an unconventional coupling of the CDW and superconducting states. Specifically, we generate a phase diagram for $CsV_3Sb_{5-x}Sn_x$ that illustrates the impact of hole-doping the system and lifting the nearest vHs toward and above E_F. Superconductivity exhibits a non-monotonic evolution with the introduction of holes, resulting in two "domes" peaked at 3.6 K and 4.1 K and the rapid suppression of three-dimensional CDW order. The evolution of CDW and superconducting order is compared with the evolution of the electronic band structure of $CsV_3Sb_{5-x}Sn_x$, where the complete suppression of superconductivity seemingly coincides with an electron-like band comprised of Sb p_z orbitals pushed above E_F.

Kagome metals naturally support electronic structures that host Dirac points, flat bands, and saddle points, leading to electronic instabilities associated with divergences in the density of states at the Fermi level. A wide array of instabilities have been predicted, ranging from bond density wave order [1, 2] to charge fractionalization [3, 4], charge density waves (CDW) [5], and superconductivity (SC) [1, 6]. As a result, the interplay between competing electronic instabilities can often be tuned *via* small changes in the band filling. For example, band fillings near $5/4$ electrons per band [1, 7–10] can populate nested van Hove singularities (vHs) that drive CDW order, and, in some limits, unconventional superconductivity.

The recently discovered class of AV_3Sb_5 (A: K, Rb, Cs) kagome metals [11] are potential realizations of this physical mechanism with each member exhibiting experimental signatures associated with CDW order [12–17] followed by the low temperature onset and coexistence of superconductivity [14, 15, 18]. Upon applying hydrostatic pressure, the CDW instability in AV_3Sb_5 is coupled to superconductivity in a seemingly unconventional fashion [19, 20], and the impact of the pressure-modified band structure on the interplay between the two states remains an open area of study. In particular, understanding the relative roles of the vHs comprised of V d-orbital states near the M-points and the electron-like band comprised of Sb-states at the Γ-point within the CDW and SC mechanisms is essential to developing a microscopic picture of how the two transitions are coupled.

Carrier doping is an appealing means of tuning these features relative to the Fermi level and probing the coupling of the CDW and SC states. Shifting the relative positions of the vHs and Γ pocket relative to E_F and probing the evolution and interplay of the CDW and SC phase transitions can provide insights into the origins of each state. A recent study on oxidized thin flakes of CsV_3Sb_5, for instance, shows that hole-doping on the Cs site can enhance T_C while also suppressing CDW order [21]. In addition, DFT calculations show that hole-doping drives the vHs in the opposite direction relative to E_F than that expected *via* external hydrostatic pressure [22]. Given that an unusual coupling between SC and CDW states was observed under variable pressure [20], a systematic study of hole-doping effects stands to provide an important experimental window into understanding this unconventional coupling.

Here the effect of hole-doping on the CDW and SC states in $CsV_3Sb_{5-x}Sn_x$ with $0 \leq x \leq 1.5$ is presented. Hole-doping is achieved *via* substitution of Sn onto the Sb sites, and, because Sn and Sb are very similar in size, this drives negligible coincident steric effects in the band structure. As holes are introduced, the CDW state is rapidly suppressed, and three-dimensional CDW order vanishes near $x = 0.06$. In parallel, SC is enhanced and reaches a maximum T_C=3.6 K at $x = 0.03$ within the CDW state before decreasing as the CDW is fully suppressed. Continued hole-doping beyond the suppression of CDW order results in a second maximum in T_C=4.1 K at $x = 0.35$ prior to bulk SC weakening and vanishing beyond $x = 0.5$. Density functional theory (DFT) calculations and nuclear quadrupolar resonance measurements establish a strong preference for Sn to occupy Sb sites within the kagome plane, and DFT models predict that Sn substitution on this site lifts the Sb p_z electron-like band at Γ above E_F coincident with the vanishing of bulk SC. Furthermore, only small changes in the energies of the vHs are predicted for doping levels sufficient to suppress signatures of CDW order, suggesting the importance of Sb-states in the stabilization of both phases.

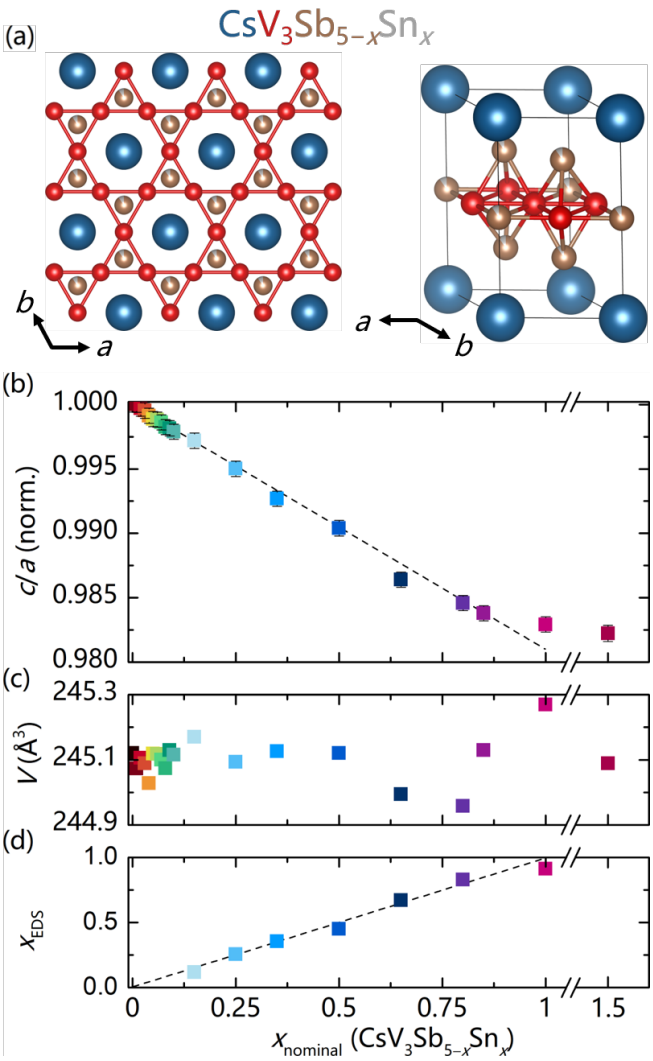

FIG. 1. (a) $CsV_3Sb_{5-x}Sn_x$ crystallizes in the parent CsV_3Sb_5 ($P6/mmm$) structure. Sn can substitute on either the Sb1 or Sb2 sublattices, and at low doping we establish a preference for the Sb site in the V kagome plane. (b-c) Sn integration into $CsV_3Sb_{5-x}Sn_x$ causes the c/a ratio to steadily decrease until the termination of solid solubility at $x = 1$. (d) For samples with concentrations above EDS sensitivity threshold, nominal Sn tracks measured Sn. Error bars are shown unless they are smaller than associated point size. The different colors correspond to sample composition and are consistent throughout the figures.

Powder samples of $CsV_3Sb_{5-x}Sn_x$ for $0 \leq x \leq 1$ in 6–7 g batches were synthesized using a combination of ball milling and high-temperature sintering [23]. Structural analysis was performed *via* synchrotron powder x-ray data acquired at Argonne National Laboratory (APS, 11-BM) and on a Panalytical Empyrean laboratory x-ray powder diffractometer. A Hitachi TM4000Plus scanning electron microscope (SEM) was used to perform energy–dispersive x-ray spectroscopy (EDS). Magnetization data were collected in a Quantum Design Magnetic Property Measurement System (MPMS) and electrical resistivity data were collected in a Quantum Design Physical Property Measurement System (PPMS). DFT calculations were performed within the Vienna ab initio Simulation Package (VASP) [24, 25], and room temperature ^{121}Sb zero-field NQR measurements were performed using a custom NMR spectrometer. Further details are available in the Supplemental Material accompanying this manuscript [23], which include references [26–34].

At room temperature, $CsV_3Sb_{5-x}Sn_x$ with $0 \leq x \leq 1$ all adopt the same hexagonal $P6/mmm$ structure as CsV_3Sb_5 with an ideal kagome network of V atoms, shown in Fig. 1(a). For $0 \leq x \leq 1$, polycrystalline samples were found to be single phase, while a secondary phase appears for $x = 1.5$, indicating the termination of the solid solution. Pawley fits of powder diffraction data were used to determine changes to the unit cell as a function of Sn content. Figures 1(b-c) show the normalized c/a ratio and the cell volume as a function of Sn content. With increasing Sn, a increases and c decreases in near perfect compensation, yielding a cell volume which is virtually independent of Sn content. Small fluctuations in volume of less than 0.16% can be explained by uncertainties in chemical composition and in the structural refinement.

The linear trend in c/a is reminiscent of a Vegard's Law-type trend, suggesting that Sn is incorporated into the parent structure as a solid solution up to approximately $x = 1$, at which point the c/a ratio plateaus. Figure 1(d) indicates that the measured Sn content (*via* EDS) tracks the nominal Sn content. While Rietveld refinements of x-ray data confirm that powders are single phase, poor scattering contrast between Sb and Sn impedes the ability to refine whether Sn is uniformly distributed on both the Sb1 and Sb2 sites, or whether there is preferential occupation of a particular sublattice. DFT calculations suggest a preference ≈ 10 meV/atom for Sn to substitute preferentially on the Sb1 (in the kagome plane) and nuclear quadropole resonance (NQR) measurements (discussed later) confirm that Sn atoms preferentially occupy this site [23].

Undoped CsV_3Sb_5 single crystals have a superconducting T_C=2.5 K [14, 21] and a charge density wave transition temperature T^*=94 K [13, 16] that drives a structural distortion into a $2 \times 2 \times 4$ enlarged unit cell; one containing layers of kagome nets distorted into both star-of-David and tri-hexagonal structures [13, 35, 36]. Polycrystalline samples show identical transition temperatures, although both transitions are broader compared to single crystals [14]. This is largely due to powders being very sensitive to exact synthesis conditions and strain effects [23]. Pure CsV_3Sb_5 powder synthesized here has an onset T_C of 2.70 K and a midpoint T_C of 2.07 K. As Sn is added within the matrix, Figure 2(a) shows the evolution of superconductivity, focusing on two different doping regimes ($x = 0$ to 0.03 and $x = 0.1$ to 0.35). All super-

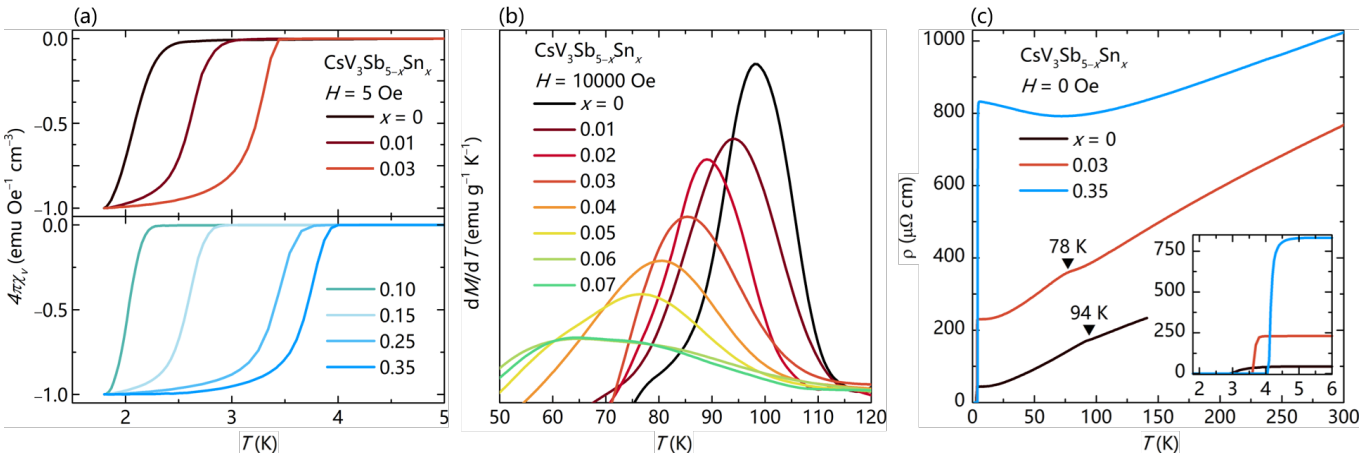

FIG. 2. (a) The superconducting T_C measured under a field of $H = 5$ Oe shows a systematic shift to higher temperature in the compositions leading to the two T_C maximums. The superconducting fraction is normalized to account for errors in mass and packing fraction so all data have a minimum of -1, the theoretical minimum. (b) dM/dT for compositions $x \leq 0.06$ show a decrease in CDW T^*, and this transition disappears for greater Sn compositions. (c) Resistivity data also show this enhancement in T_C, and the low-T, normal state resistivity for $x = 0.35$ is about 4 times higher than $x = 0.03$.

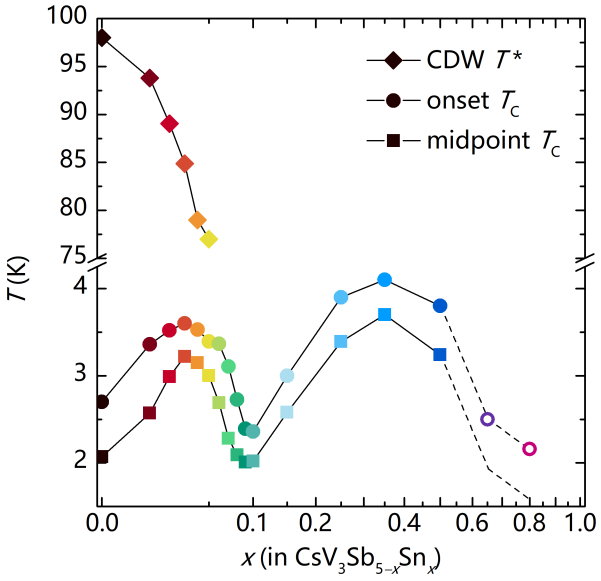

FIG. 3. Hole-doping phase diagram for $CsV_3Sb_{5-x}Sn_x$. The double-dome structure is clearly evident, as is the depression of the CDW ordering temperature. T_C shows two maxima at $x = 0.03$ and at $x = 0.35$ and the CDW state disappears by $x = 0.06$. We note that the first T_C maximum occurs while the CDW is still present, and the CDW vanishes once T_C is already declining again $x > 0.03$. For $x \geq 0.65$, the volume fraction of superconductivity decreases and the onset T_Cs are represented with open circles.

conducting samples show $4\pi\chi_v \approx -1$ in magnetization. Fractions slightly exceeding unity are attributed to errors in the packing density, and data are normalized to -1 for ease of comparison. The effect of Sn on T_C becomes immediately apparent: as the Sn content is increased to $x = 0.03$, T_C increases to a local maxima of 3.6 K. T_C then decreases with continued hole-doping, followed by a second superconducting dome appearing shortly thereafter with a maximum $T_C = 4.1$ K at x=0.35. Superconductivity assumes only a partial volume fraction for $x > 0.5$, and the SC state completely disappears by $x = 0.85$. An exhaustive set of susceptibility measurements is provided in the supplemental information [23].

The evolution of CDW order upon hole-doping can be monitored via the inflection point in magnetization that appears at the CDW onset. Using the peak in dM/dT as a metric for the onset of three-dimensional CDW order, Fig. 2(b) shows that light hole substitution causes the CDW transition to rapidly broaden and shift to lower temperatures. Undoped, the peak in dM/dT is 98.01 K and this peak decreases to less than 80 K at x=0.04. For $x > 0.05$, signatures of the CDW transition in magnetization cannot be resolved, although it is possible that a highly broadened CDW anomaly smoothly continues its rapid suppression with higher Sn doping. Despite the ambiguity in the precise position of CDW phase boundary near x=0.05, the superconducting and CDW states clearly coexist at the first maximum of the first superconducting dome ($x = 0.03$). This is distinct from the second maximum in T_C at higher Sn content ($x = 0.35$), which occurs far beyond the apparent suppression of CDW order. Future work studying single crystals will be required to fully map if the suppression of the CDW state is a first or second order phase boundary and to fully explore whether CDW order is becoming short-ranged at larger Sn-doping levels.

Figure 2(c) shows electrical resistivity measurements performed on samples at both peak T_C values (x =0.03 and x =0.35). Zero-resistivity conditions agree well with the T_C obtained *via* magnetization measurements, and

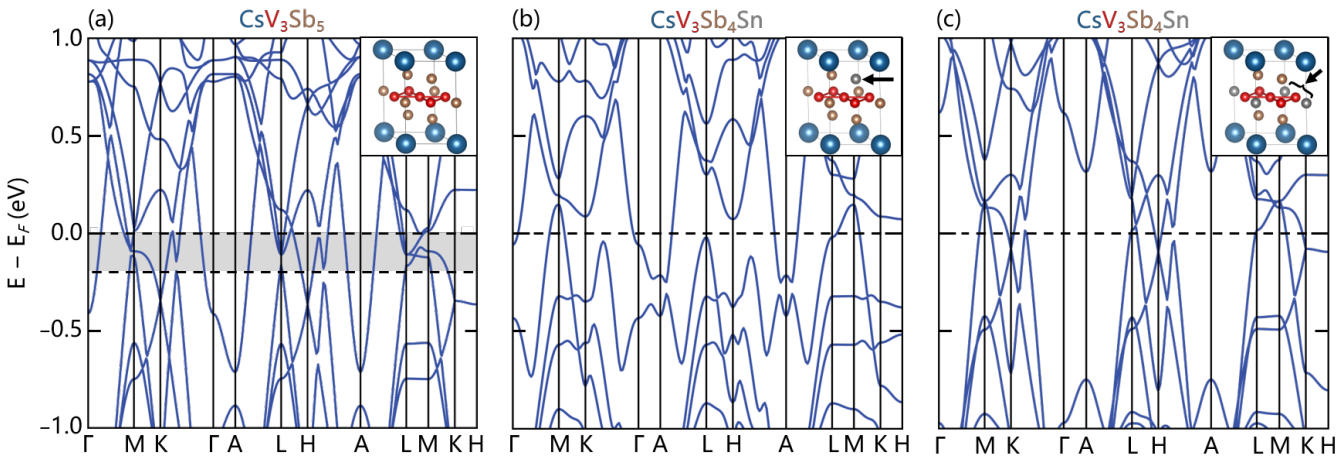

FIG. 4. (a) DFT calculations for CsV_3Sb_5 highlighting the allowable range of Fermi levels under the rigid band approximation for substitution of one Sn atom per formula unit. (b) Calculation of the band structure of CsV_3Sb_4Sn where one Sn has been substituted within the kagome plane. Here the majority of the electronic structure is preserved with the exception of the Γ pocket, where the occupied Sb band is replaced with an unoccupied Sn band above E_F. (c) Calculation of the band structure of CsV_3Sb_4Sn where one Sn has been substituted at a Sb site outside of the kagome plane (OKP). A strong reconstruction of many bands can be observed, in particular near K, H, and K-Γ.

the CDW onset temperature is further marked for the sample with $x = 0.03$. The resistance immediately prior to the onset of SC increases quite dramatically upon Sn substitution, from 50 $\mu\Omega$-cm ($x = 0$), to 250 $\mu\Omega$-cm ($x = 0.03$, first T_C peak), to 800 $\mu\Omega$-cm ($x = 0.35$, second T_C peak), and the temperature dependence of the resistivity, particularly near the CDW temperature, changes dramatically with Sn doping. As a summary, Figure 3 plots a phase diagram showing the effect of Sn-substitution on both SC and CDW orders. A two-dome structure is immediately evident in T_C, as is the relatively rapid suppression of CDW order with the introduction of Sn.

The CsV_3Sb_5 lattice supports nearly 1/5 of the total Sb being replaced by Sn. To give a rough sense of the range over which E_F can be tuned, Figure 4(a) shows the electronic structure of pure CsV_3Sb_5 along with the range of Fermi levels achievable with a loss of 1 electron per unit cell (gray shaded region). In a rigid band shift approximation, substitution of Sn should allow E_F to be tuned across multiple vHs and Dirac points near the M- and K-points, respectively. However, reconstruction of the bands associated with the Sb orbitals and orbital selective doping effects are expected, and Figure 4(c) shows one hypothetical structure with Sn substituted on the Sb2 sublattice (out of the kagome plane). Here, in addition to the expected shift of the Fermi level (note the position of the M-point vHs crossing now ≈ 0.2 eV *above* E_F), a significant reconstruction is also resolved around the K, L, and H points. Notably, the electron-like band at Γ is preserved in this $x = 1$ structure. Alternatively, if Sn substitution instead occupies the Sb1 sublattice within the kagome plane, the overall electronic structure relative to CsV_3Sb_5 is largely preserved and mimics a rigid band shift model, with the important exception of the Sb-derived Γ-pocket, which vanishes and is replaced with an electron-like Sn-band far above E_F. Colorized orbital contributions to the band structure structures shown in Fig. 4 are presented in the supplemental information [23].

To clarify the impact of Sn-doping on the band structure, NQR measurements were performed and establish that Sn preferentially occupies the Sb1 sites in the kagome plane [23]. This is consistent with DFT calculations that show a small energy preference for Sn occupying the Sb1 site. With this doping-site established, supercell calculations at fractional in-plane Sb substitution were performed and show that, as Sn content is increased, the electron-like band at Γ lifts above E_F near $x = 0.5$ in tandem with the disappearance of bulk superconductivity [23]. This suggests that superconductivity in CsV_3Sb_5 in-part relies on the Sb p_z-derived orbitals, and aligns with results of earlier pressure studies [37].

At smaller Sn-doping levels, the observation of an intermediate peak in T_C demonstrates a complex interplay between the Sb-states at Γ and the V d-states driving the CDW order. Supercell calculations show a rather mild shift in the M-point vHs from roughly -0.072 eV below E_F for x=0 to -0.047 eV for x=0.33 and -0.042 eV for x=0.5, prior to shifting 0.083 eV above E_F in x=1. The small shift in the expected energies of the vHs toward E_F under mild x=0.05 substitution fails to explain the rapid suppression of the CDW state at this doping, suggesting a complicated balance of energy scales underpinning the CDW state. This is consistent with the rapid suppression of the CDW state under hydrostatic pressure [19, 20]; however the two SC domes apparent under hole-doping

seem distinct from those realized under pressure. Superconductivity in crystals nominally doped between the SC domes retains a sharp transition [23], unlike the weak SC observed in pressure studies. Further work exploring the distinctions between pressure (pushing vHs away from E_F) and hole-doping (pulling vHs toward E_F) is required to fully explore the parallels between the hole-doping and pressure-driven phase diagrams.

Hole-doping realized *via* chemical substitution of Sn into CsV_3Sb_5 results in a complex electronic phase diagram featuring two SC domes – one that coexists with CDW order and a second that appears following the suppression of the CDW state. Unconventional superconductivity has been predicted for fillings slightly away from the vHs [8]. The peak in T_C prior to the suppression of CDW order and the subsequent, second peak in T_C following the complete suppression of the CDW state motivates deeper theoretical studies into how the Sb p_z states intertwine with both CDW order SC in these materials. Our results demonstrate that small changes in the electronic structure achieved through carrier doping can have dramatic impacts on SC and CDW orders in CsV_3Sb_5 and provide a elegant chemical means to tune the competition between these states in the new AV_3Sb_5 class of kagome superconductors.

ACKNOWLEDGMENTS

This work was supported by the National Science Foundation (NSF) through Enabling Quantum Leap: Convergent Accelerated Discovery Foundries for Quantum Materials Science, Engineering and Information (Q-AMASE-i): Quantum Foundry at UC Santa Barbara (DMR-1906325). The research reported here made use of shared facilities of the NSF Materials Research Science and Engineering Center at UC Santa Barbara DMR-1720256, a member of the Materials Research Facilities Network (www.mrfn.org). Use of the Advanced Photon Source at Argonne National Laboratory was supported by the U.S. Department of Energy, Office of Science, Office of Basic Energy Sciences, under Contract No. DE-AC02-06CH11357. YMO is supported by the National Science Foundation Graduate Research Fellowship Program under Grant No. DGE-1650114. BRO is supported by the California NanoSystems Institute through the Elings Fellowship program. FK acknowledges the Roy T. Eddleman Center for Quantum Innovation (ECQI) for their support. Work at Brown was supported in part by the the National Science Foundation grant No. DMR-1905532 and funds from Brown and University of Bologna.

REFERENCES

* yoey@ucsb.edu, stephendwilson@ucsb.edu

[1] W.-S. Wang, Z.-Z. Li, Y.-Y. Xiang, and Q.-H. Wang, Competing electronic orders on kagome lattices at van Hove filling, Phys. Rev. B **87**, 115135 (2013).

[2] S. V. Isakov, S. Wessel, R. G. Melko, K. Sengupta, and Y. B. Kim, Hard-core bosons on the kagome lattice: Valence-bond solids and their quantum melting, Phys. Rev. Lett. **97**, 147202 (2006).

[3] A. O'Brien, F. Pollmann, and P. Fulde, Strongly correlated fermions on a kagome lattice, Phys. Rev. B **81**, 235115 (2010).

[4] A. Rüegg and G. A. Fiete, Fractionally charged topological point defects on the kagome lattice, Phys. Rev. B **83**, 165118 (2011).

[5] H.-M. Guo and M. Franz, Topological insulator on the kagome lattice, Phys. Rev. B **80**, 113102 (2009).

[6] W.-H. Ko, P. A. Lee, and X.-G. Wen, Doped kagome system as exotic superconductor, Phys. Rev. B **79**, 214502 (2009).

[7] S.-L. Yu and J.-X. Li, Chiral superconducting phase and chiral spin-density-wave phase in a Hubbard model on the kagome lattice, Phys. Rev. B **85**, 144402 (2012).

[8] M. L. Kiesel, C. Platt, and R. Thomale, Unconventional Fermi surface instabilities in the kagome Hubbard model, Phys. Rev. Lett. **110**, 126405 (2013).

[9] K. Barros, J. W. Venderbos, G.-W. Chern, and C. Batista, Exotic magnetic orderings in the kagome Kondo-lattice model, Phys. Rev. B **90**, 245119 (2014).

[10] X. Feng, K. Jiang, Z. Wang, and J. Hu, Chiral flux phase in the Kagome superconductor AV_3Sb_5, Sci. Bull. (2021).

[11] B. R. Ortiz, L. C. Gomes, J. R. Morey, M. Winiarski, M. Bordelon, J. S. Mangum, I. W. Oswald, J. A. Rodriguez-Rivera, J. R. Neilson, S. D. Wilson, *et al.*, New kagome prototype materials: discovery of KV_3Sb_5, RbV_3Sb_5, and CsV_3Sb_5, Phys. Rev. Mater. **3**, 094407 (2019).

[12] Y.-X. Jiang, J.-X. Yin, M. M. Denner, N. Shumiya, B. R. Ortiz, G. Xu, Z. Guguchia, J. He, M. S. Hossain, X. Liu, *et al.*, Unconventional chiral charge order in kagome superconductor KV_3Sb_5, Nat. Mater. , 1 (2021).

[13] H. Zhao, H. Li, B. R. Ortiz, S. M. Teicher, T. Park, M. Ye, Z. Wang, L. Balents, S. D. Wilson, and I. Zeljkovic, Cascade of correlated electron states in the kagome superconductor CsV_3Sb_5, Nature **599**, 216 (2021).

[14] B. R. Ortiz, S. M. Teicher, Y. Hu, J. L. Zuo, P. M. Sarte, E. C. Schueller, A. M. Abeykoon, M. J. Krogstad, S. Rosenkranz, R. Osborn, R. Seshadri, L. Balents, J. He, and S. D. Wilson, CsV_3Sb_5: A $\mathbb{Z}_2$ topological kagome metal with a superconducting ground state, Phys. Rev, Lett. **125**, 247002 (2020).

[15] B. R. Ortiz, P. M. Sarte, E. M. Kenney, M. J. Graf, S. M. Teicher, R. Seshadri, and S. D. Wilson, Superconductivity in the $\mathbb{Z}_2$ kagome metal KV_3Sb_5, Phys. Rev. Mater. **5**, 034801 (2021).

[16] Z. Liang, X. Hou, F. Zhang, W. Ma, P. Wu, Z. Zhang, F. Yu, J.-J. Ying, K. Jiang, L. Shan, *et al.*, Three-dimensional charge density wave and surface-dependent vortex-core states in a kagome superconductor CsV_3Sb_5, Physical Review X **11**, 031026 (2021).

[17] H. Chen, H. Yang, B. Hu, Z. Zhao, J. Yuan, Y. Xing, G. Qian, Z. Huang, G. Li, Y. Ye, *et al.*, Roton pair density wave in a strong-coupling kagome superconductor, Nature **599**, 222 (2021).

[18] Q. Yin, Z. Tu, C. Gong, Y. Fu, S. Yan, and H. Lei, Superconductivity and normal-state properties of kagome metal RbV_3Sb_5 single crystals, Chinese Phys. Lett. **38**, 037403 (2021).

[19] F. Du, S. Luo, B. R. Ortiz, Y. Chen, W. Duan, D. Zhang, X. Lu, S. D. Wilson, Y. Song, and H. Yuan, Pressure-induced double superconducting domes and charge instability in the kagome metal KV_3Sb_5, Phys. Rev. B **103**, L220504 (2021).

[20] K. Chen, N. Wang, Q. Yin, Y. Gu, K. Jiang, Z. Tu, C. Gong, Y. Uwatoko, J. Sun, H. Lei, *et al.*, Double superconducting dome and triple enhancement of T_C in the kagome superconductor CsV_3Sb_5 under high pressure, Phys. Rev. Lett. **126**, 247001 (2021).

[21] Y. Song, T. Ying, X. Chen, X. Han, X. Wu, A. P. Schnyder, Y. Huang, J.-g. Guo, and X. Chen, Competition of Superconductivity and Charge Density Wave in Selective Oxidized CsV_3Sb_5 Thin Flakes, Physical review letters **127**, 237001 (2021).

[22] H. LaBollita and A. S. Botana, Tuning the Van Hove singularities in AV_3Sb_5 (A= K, Rb, Cs) via pressure and doping, Physical Review B **104**, 205129 (2021).

[23] See Supplemental Information for further details.

[24] G. Kresse and J. Furthmüller, Efficient iterative schemes for ab initio total-energy calculations using a plane-wave basis set, Phys. Rev. B **54**, 11169 (1996).

[25] G. Kresse and J. Furthmüller, Efficiency of ab-initio total energy calculations for metals and semiconductors using a plane-wave basis set, Comput. Mater. Sci. **6**, 15 (1996).

[26] A. A. Coelho, TOPAS and TOPAS-Academic: An optimization program integrating computer algebra and crystallographic objects written in C++, J. Appl. Crystallogr. **51**, 210 (2018).

[27] G. W. Stinton and J. S. Evans, Parametric Rietveld refinement, J. Appl. Crystallogr. **40**, 87 (2007).

[28] K. Momma and F. Izumi, VESTA 3 for three-dimensional visualization of crystal, volumetric and morphology data, J. Appl. Crystallogr. **44**, 1272 (2011).

[29] A. Abragam, *The principles of nuclear magnetism*, 32 (Oxford University Press, 1961).

[30] P. E. Blöchl, Projector augmented-wave method, Phys. Rev. B **50**, 17953 (1994).

[31] G. Kresse and D. Joubert, From ultrasoft pseudopotentials to the projector augmented-wave method, Phys. Rev. B **59**, 1758 (1999).

[32] W. Setyawan and S. Curtarolo, High-throughput electronic band structure calculations: Challenges and tools, Comp. Mater. Sci. **49**, 299 (2010).

[33] A. M. Ganose, A. J. Jackson, and D. O. Scanlon, sumo: Command-line tools for plotting and analysis of periodic *ab initio* calculations, J. Open Source Softw. **3**, 717 (2018).

[34] J. Luo, Z. Zhao, Y. Zhou, J. Yang, A. Fang, H. Yang, H. Gao, R. Zhou, and G.-q. Zheng, Possible star-of-David pattern charge density wave with additional modulation in the kagome superconductor CsV_3Sb_5, npj Quantum Materials **7**, 1 (2022).

[35] B. R. Ortiz, S. M. Teicher, L. Kautzsch, P. M. Sarte, N. Ratcliff, J. Harter, J. P. Ruff, R. Seshadri, and S. D. Wilson, Fermi surface mapping and the nature of charge density wave order in the kagome superconductor CsV_3Sb_5, Physical Review X **11**, 041030 (2021).

[36] Y. Hu, X. Wu, B. R. Ortiz, X. Han, N. C. Plumb, S. D. Wilson, A. P. Schnyder, and M. Shi, Coexistence of Tri-Hexagonal and Star-of-David Pattern in the Charge Density Wave of the Kagome Superconductor AV_3Sb_5, arXiv preprint arXiv:2201.06477 (2022).

[37] A. Tsirlin, P. Fertey, B. R. Ortiz, B. Klis, V. Merkl, M. Dressel, S. Wilson, and E. Uykur, Role of Sb in the superconducting kagome metal CsV_3Sb_5 revealed by its anisotropic compression, SciPost Physics **12**, 049 (2022).

Fermi level tuning and double-dome superconductivity in the kagome metals $CsV_3Sb_{5-x}Sn_x$

Yuzki M. Oey,[1] Brenden R. Ortiz,[1] Farnaz Kaboudvand,[1] Jonathan Frassineti,[2,3] Erick Garcia,[2] Rong Cong,[2] Samuele Sanna,[3] Vesna F. Mitrović,[2] Ram Seshadri,[1] and Stephen D. Wilson[1]

[1]*Materials Department, Materials Research Laboratory, and California NanoSystems Institute University of California Santa Barbara, California 93106 United States**

[2]*Department of Physics, Brown University, Providence, RI 02912, U.S.A.*

[3]*Department of Physics and Astronomy "A. Righi", University of Bologna, I-40127 Bologna, Italy*

(Dated: March 4, 2022)

METHODS

Elemental Cs (liquid, Alfa 99.98%), V (powder, Sigma 99.9%), Sb (shot, Alfa 99.999%), and Sn (shot, Alfa 99.9999%). Stoichiometric quantities were weighed in an argon glove box with oxygen and water levels of $<$ 0.5 ppm. Vanadium powder was cleaned prior to the synthesis using EtOH and concentrated HCl to remove residual oxides. Elements were loaded in a tungsten carbide ball mill vial and milled for 60 min in a SPEX 8000D high-energy ball mill. Resulting powders were ground in agate, sieved through a 106 micron sieve, sealed in fused silica, and annealed at 823 K for 48 K. A secondary grind and anneal (723 K, 12 h) was utilized to ensure best superconducting fractions and Sn homogenity. The resulting powder is dark grey and air stable.

High–resolution synchrotron powder X–ray data were acquired at Argonne National Laboratory (APS, 11-BM) with an average wavelength of $\lambda = 0.458$ Å. Powders were diluted with ground silica before packing in 0.8 mm kapton capillaries to reduce X-ray absorption. Additional powder X–ray (pXRD) data were collected on a Panalytical Empyrean powder diffractometer equipped with a PIXcel 1D detector. Topas Academic[1] was used to refine the patterns with Pawley and Rietveld fitting,[2] and crystal structures were visualized using VESTA.[3] A Hitachi TM4000Plus scanning electron microscope (SEM) was used to perform energy–dispersive X–ray spectroscopy (EDS). The AztecOne software was used to analyze and obtain the chemical composition in higher Sn content samples.

A Quantum Design Magnetic Property Measurement System (MPMS) with a vibrating sample magnetometer (VSM) was used to take magnetization data. Approximately 15 mg of powder was packed in a plastic VSM capsule and loaded in a brass rod sample holder. Superconductivity measurements utilized an applied field of 5 Oe. Due to the intrinsically low moment of CsV_3Sb_5, temperature–depenedent CDW measurements utilized a higher field of $H = 10000$ Oe. A Quantum Design Physical Property Measurement System (PPMS) Dynacool was used for resistivity measurements. Resistivity measurements were performed using a standard 4-point contact geometry. Silver paint and gold wire were used to make electrical contact to sintered, pressed bars of CsV_3Sb_5. The electrical transport option was used with a constant frequency of $\sim$15 Hz and a current of 1 mA.

The room temperature ^{121}Sb zero field nuclear quadrupolar resonance (NQR) measurements were done at Brown University. The NQR data was recorded using a state-of-the-art laboratory-made NMR spectrometer. The spectra were obtained, at each given value of frequency, from Fourier transforms of the spin-echo. We used a standard spin echo sequence $(\pi/2 - \tau - \pi)$. A $\pi/2$ pulse that optimized signal intensity of 3.4 μs was used. The shape of the spectra presented in the manuscript are independent of the duration of time interval τ. The NQR relaxation rate T_1^{-1} was measured using a Spin Stimulated Echo 3-pulse sequence $(\pi/2 - \tau - \pi/2 - \tau_d - \pi/2)$ to obtain magnetization recovery curves $M(\tau_d)$. The resulting value of the rate was obtained by fitting the magnetization to a single exponential function of time $M(\tau_d) \propto \exp(-t/T_1)$. Since the nuclear spin I of ^{121}Sb equals to $5/2$ and both Sb sites (Sb1 and Sb2) are in non-cubic environments, two distinct quadrupolar lines are observed per site [4]. The shift was obtained from the frequency of the first moment of spectral distribution.

For electronic state calculations, first-principles calculations based on density functional theory (DFT) within the Vienna ab initio Simulation Package (VASP) were performed.[5, 6] The projector augmented wave (PAW) method[7, 8] was employed and relaxations of the ionic positions were conducted using an energy cutoff of 520 eV. Reciprocal space k-point meshes were automatically generated at a density of 55 Å–1 along each reciprocal lattice vector. The band structure was calculated across the main paths along the high symmetry points as defined by Setyawan and Curtarolo.[9] Density of states (DOS) and band structures were visualized using the sumo package.[10] The CsV_3Sb_5 structure has 5 sites for Sb atoms. Two sites are unique and symmetrically distinct: within the kagome plane (WKP), and out of the kagome plane (OKP). In this study we calculated both cases of when Sn is WKP and when Sn is in one of the OKP sites.

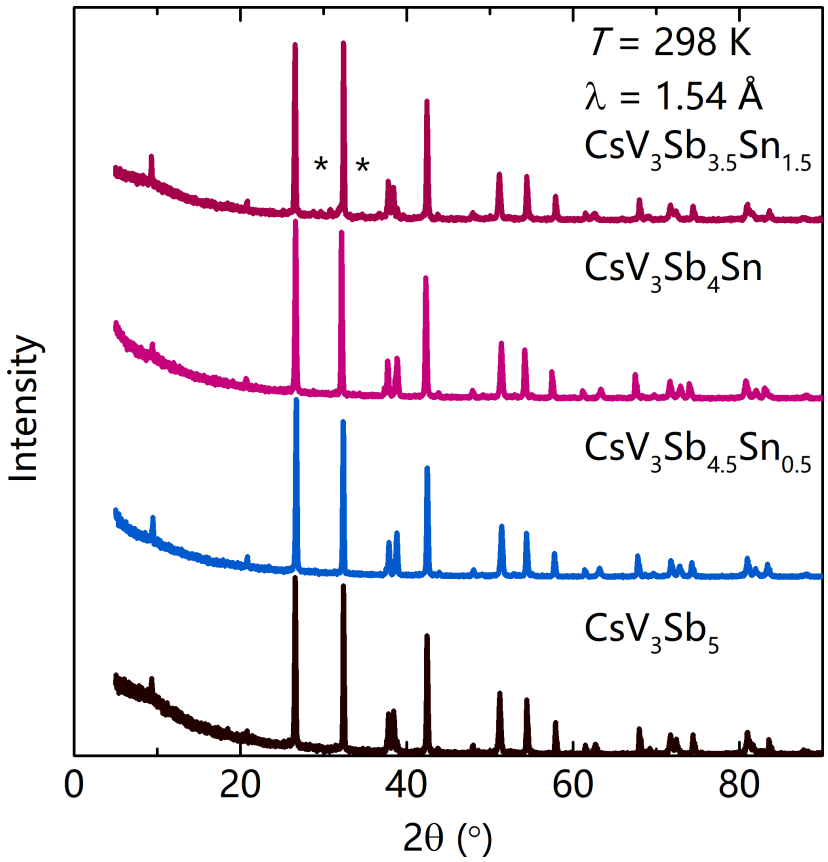

SFIG 1. Powder X–ray diffraction on samples of $CsV_3Sb_{5-x}Sn_x$ for $x = 0$, 0.5, 1.0, and 1.5. Compositions of $x \leq 1$ show single phase samples. A small secondary phase appears for $x = 1.5$, as indicated by the asterisks (*).

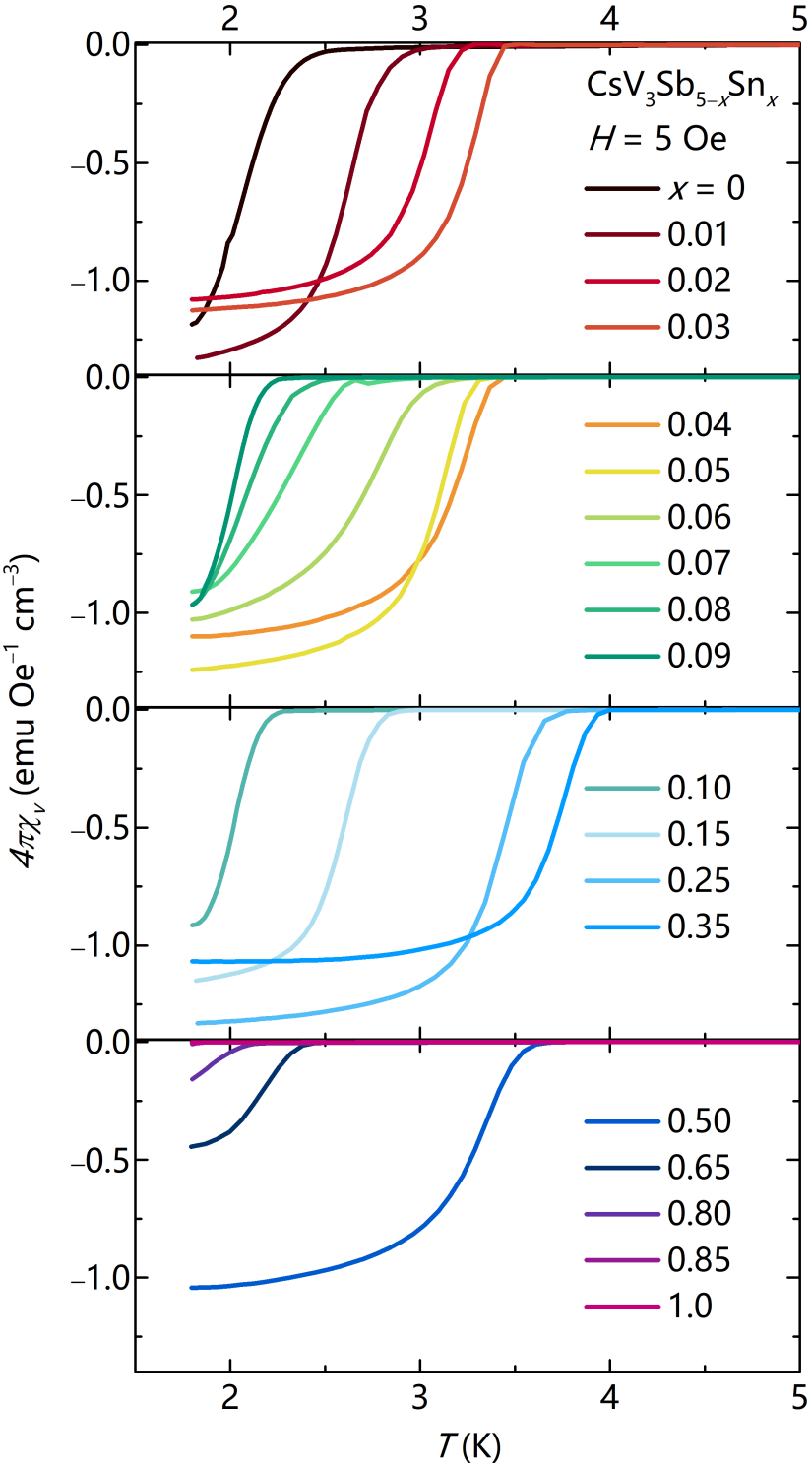

SFIG 2. Susceptibility measurements ($H = 5$ Oe) on powders of $CsV_3Sb_{5-x}Sn_x$ for $0 \leq x \leq 1.0$ show that the superconducting fractions, calculated as $4\pi\chi_v$, are ≈ 1 for $x \leq 0.50$. From $x \geq 0.65$, the superconducting fraction decreases, and superconductivity is fully suppressed by $x = 1$.

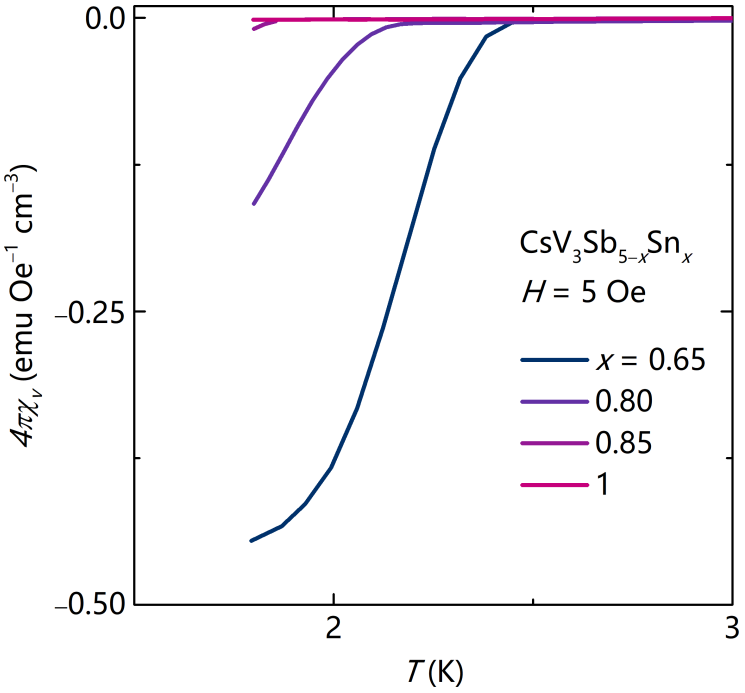

SFIG 3. Susceptibility measurements on powders of $CsV_3Sb_{5-x}Sn_x$ for $x \geq 0.65$ show that the superconducting fraction significantly diminishes. By $x = 1$, there is no trace of superconductivity at 1.8 K. However, it is not clear whether the superconductivity is being suppressed with the higher amounts of Sn doping or if the T_C is below 1.8 K.

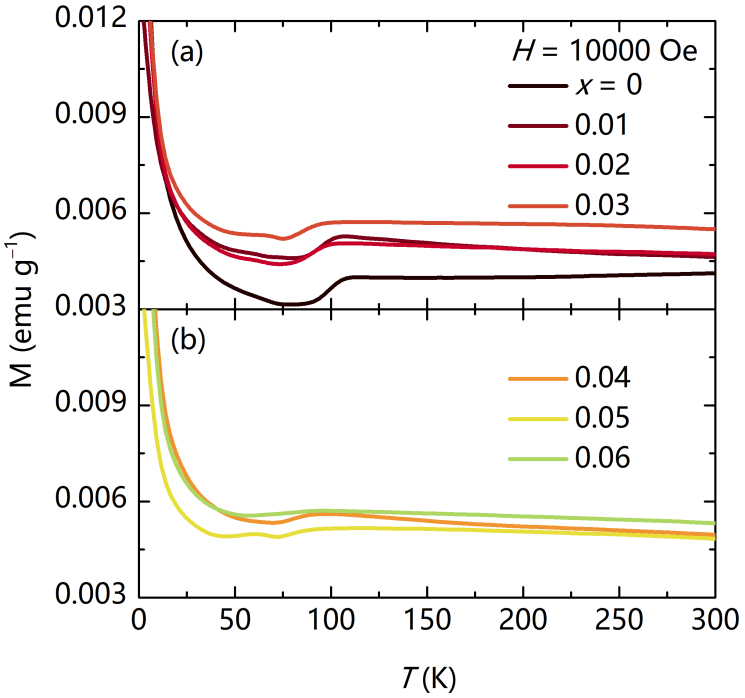

SFIG 4. Magnetization measurements on powders of $CsV_3Sb_{5-x}Sn_x$ ($H = 10000$ Oe) show the suppression of the CDW order by $x = 0.06$. For visual clarity, the datasets are split. Although there is a clear inflection point for $0 \leq x \leq 0.04$, the magnitude of the CDW order significantly decreases and T^* shifts to lower temperature. The additional inflection for $x = 0.05$ at around 55 K can be attributed to oxygen contamination in the chamber of the instrument.

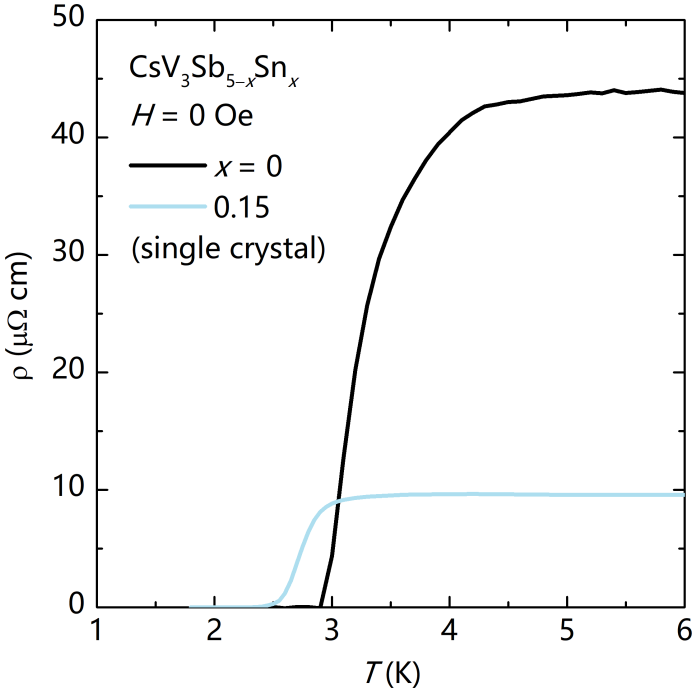

SFIG 5. Resistivity data on single crystal $CsV_3Sb_{4.85}Sn_{0.15}$ complements powder resistivity data in the main text and shows no broadening in the superconducting transition.

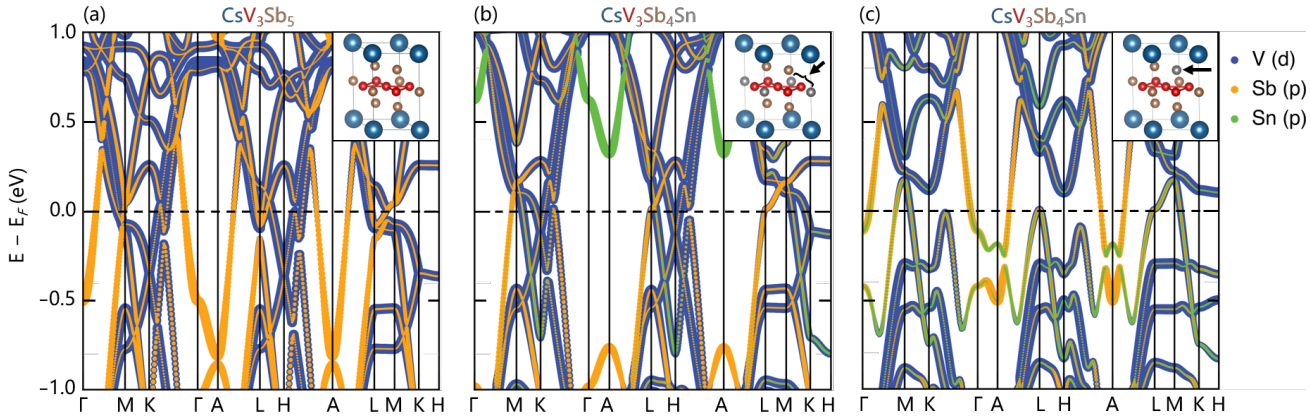

SFIG 6. Colorized bands from DFT calculations show the orbital contributions from V, Sb, and Sn. (a) The Γ pocket in CsV_3Sb_5 is from the Sb p_z orbitals. (b) However, the fully substituted structure with Sn in the kagome plane arises from the Sn p_z orbitals.

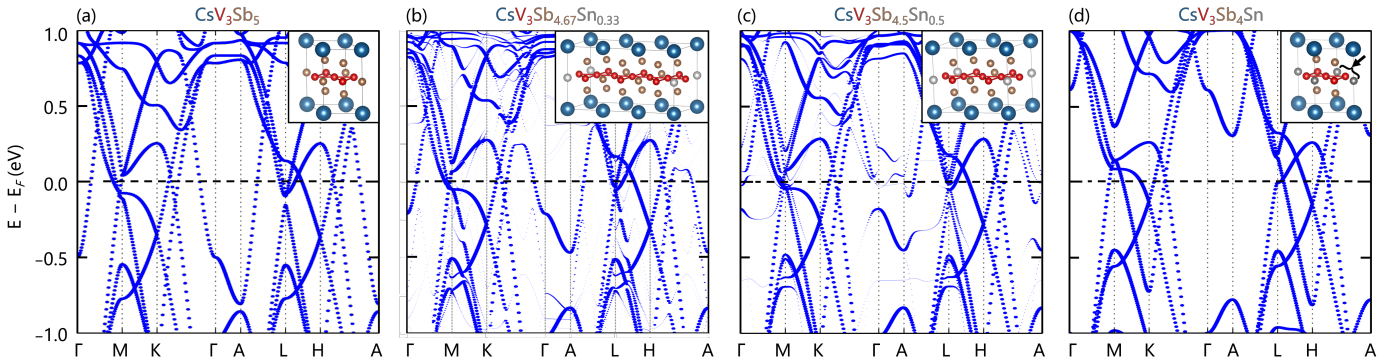

SFIG 7. Supercell DFT calculations for $x = 0.33$ and 0.5 show the evolution of bands as Sn content is increased. The Γ pocket lifts through E_F by $x = 0.5$ while the van Hove singularity at the M point crosses E_F by $x = 1$.

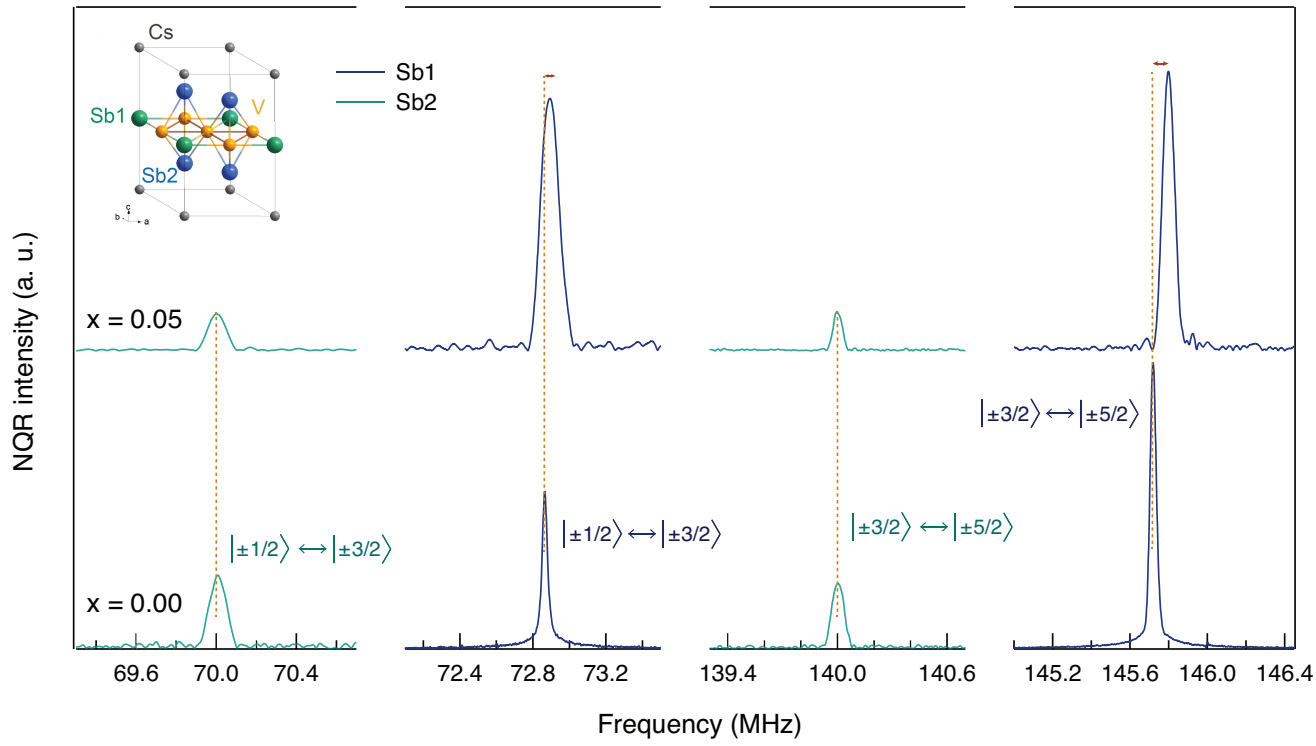

SFIG 8. Sn doping dependence of the NQR spectra for two different Sn concentrations, as denoted. Dashed lines denote position of all the spectral lines of undoped sample. Sb site assignment is depicted in the inset.

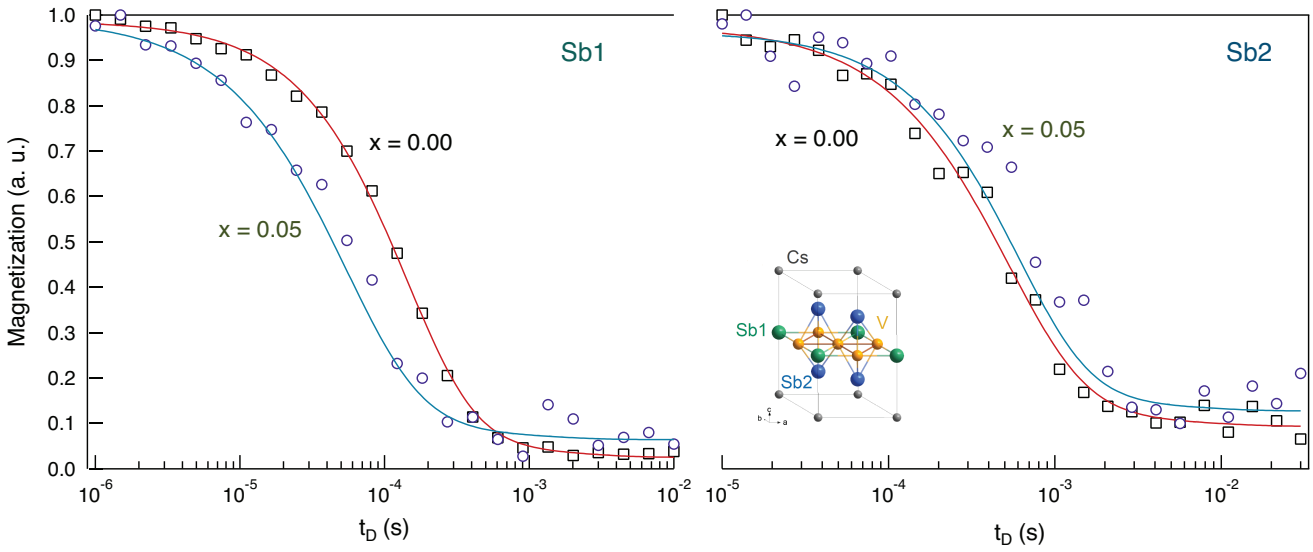

SFIG 9. Nuclear magnetization recovery curves following $\pi/2$ pulse excitation for two Sn doping concentrations, $x = 0$ and $x = 0.05$, for two Sb sites. Sb site assignment is depicted in the inset. Solid lines are fits to the exponential function used to deduce the NMR rate T_1^{-1}.

Sb site	Sn concentration	ν_Q (MHz)
Sb1	0.00	140.0024 ± 0.0012
Sb1	0.05	139.9963 ± 0.0012
Sb2	0.00	145.7197 ± 0.0012
Sb2	0.05	145.7988 ± 0.0012

TABLE I. Doping dependence of the frequency shift of the quadrupolar line for $|\pm 5/2\rangle \leftrightarrow |\pm 3/2\rangle$ transition, for both Sb sites, at room temperature.

Sb site	Sn concentration	T_1 (ms)
Sb1	0.00	6.23 ± 0.44
Sb1	0.05	6.24 ± 0.49
Sb2	0.00	1.87 ± 0.05
Sb2	0.05	1.63 ± 0.09

TABLE II. Relaxation time T_1 for Sb1 and Sb2 sites for two different Sn doping concentrations.

Supplementary Note 1: ^{121}Sb NQR Spectra and Shift

In Supplementary Figure S8 we plot the doping dependence of the NQR frequency spectra for ^{121}Sb sites 1 and 2. In addition, in Supplementary Table SI, we summarize the frequency shift associated with the first moment of Sb site 1 and 2 for two Sn doping concentrations. Evidently, only the Sb2 site line shifts when Sn dopants are added to the sample, while the Sb1 spectra remain at a fixed frequency position, unaffected by Sn doping. Naively, one could conclude that this observation implies that NQR measurements indicate that Sn dopants only occupy Sb2 sites. However, taking into careful consideration the crystalline structure shown in Supplementary Figure S8 and the distances between different Sb sites, we conclude that the observed shift in the quadrupolar frequency of Sb2 sites, can only be accounted for if a low concentration of the Sn dopants replace the in-plane Kagome Sb1 sites.

Specifically, the distances between the Sb1-Sb1 sites are much larger than that between the Sb1-Sb2 ones. Therefore, a substitution of Sn into Sb1 nuclear sites will only affect Sb2 nuclei, since Sb2 nuclei experience a more drastically modified electronic charge distribution, *i.e.* the Electric Field Gradient (EFG) tensor, around them, resulting in a different observed quadrupolar coupling. In the other case, a dopant in Sb2 sites would affect both Sb1 and Sb2 sites, since Sb1-Sb2 and Sb2-Sb2 distances are comparable. If this was the case, an appreciable shift of the quadrupolar frequency should also have been observed for Sb1 sites.

Supplementary Note 2: ^{121}Sb NQR Relaxation Rate

In the absence of magnetic correlation, the NMR relaxation rate is given by

$$\frac{1}{T_1} \propto \int d\varepsilon \, N_\uparrow(\varepsilon) N_\downarrow(\varepsilon) f(\varepsilon)[1 - f(\varepsilon)], \qquad (1)$$

where $N_\downarrow$ and $N_\uparrow$ denote the densities of up- and down-spin states and $f(\varepsilon)$ is the Fermi occupation function. That is, $(T_1)^{-1}$ is proportional to the square of the DOS integrated over energy ε in the range of the order of $k_B T$ around E_F selected by the Fermi function. In Supplementary Figure S9 we plot the magnetization recovery curves used to deduce the relaxation rate for both Sb sites. The values of the rate are summarized in Supplementary Table II. For the Sb1 site the relaxation rate is independent on Sn concentration, within the error bars. However, the Sb2 relaxation rate varies as a function of doping. The above equation implies that the $(T_1)^{-1}$ is proportional to the square of the DOS at the Fermi level. A comparison of the $(T_1)^{-1}$ for the two concentrations at the Sb2 site indicate that the DOS in the $x = 0.05$ sam-

ple increased by 5.5% compared to that in the undoped $x = 0.0$ sample.

Supplementary Note 3: Quadrupolar effects

In the simplest case of zero field NQR, the interaction between eq, the electric field gradient (EFG), and the nucleus, with spin I and the quadrupole moment Q, is described by the Quadrupole Hamiltonian,

$$\mathcal{H}_{\mathrm{Q}} = \frac{(eQ)(eq)}{4I(2I-1)}[3I_z^2 - I(I+1)]. \quad (2)$$

For nuclear spin $I = 5/2$, as is the case of ^{121}Sb, the energy eigenstates of $\mathcal{H}_{\mathrm{Q}}$ are given by,

$$E = \frac{(eQ)(eq)}{4I(2I-1)}\left[3m^2 - I(I+1)\right] \quad (3)$$

The quadrupole Hamiltonian expressed in the coordinate system defined by the principal axes of the EFG, is given by,

$$\mathcal{H}_{\mathrm{Q}}(x,y) = \frac{eQV_{zz}}{4I(2I-1)}\left[(3\hat{I}_z^2 - \hat{I}^2) + \eta(\hat{I}_x^2 - \hat{I}_y^2)\right], \quad (4)$$

where $\eta \equiv |V_{xx} - V_{yy}|/V_{zz}$ is the asymmetry parameter and V_{xx}, V_{yy}, and V_{zz} are the diagonal components of the EFG. Here, V_{zz} is defined as the principle component of the EFG and $|V_{xx}| < |V_{yy}| < |V_{zz}|$, by convention.

From [4], for $I = 5/2$ and for an asymmetry parameter $\eta = 0$, there are two lines corresponding to the transitions $|3/2\rangle \rightarrow |1/2\rangle$ and $|5/2\rangle \rightarrow |3/2\rangle$, given by

$$\nu'_{5/2} = \frac{3}{20}\frac{e^2qQ}{h} \qquad \& \qquad \nu''_{5/2} = 2\nu'_{5/2}, \quad (5)$$

respectively. We observed this to be true in our case for both Sb1 and Sb2 sites at room temperature in the pure sample ($x = 0$), $\nu''_{5/2} = 2\nu'_{5/2}$. Therefore, $\eta_{Sb1} = \eta_{Sb2} = 0$, in agreement with [11].

* yoey@ucsb.edu, stephendwilson@ucsb.edu

[1] A. A. Coelho, J. Appl. Crystallogr. **51**, 210 (2018).
[2] G. W. Stinton and J. S. Evans, J. Appl. Crystallogr. **40**, 87 (2007).
[3] K. Momma and F. Izumi, J. Appl. Crystallogr. **44**, 1272 (2011).
[4] A. Abragam, *The principles of nuclear magnetism*, 32 (Oxford University Press, 1961).
[5] G. Kresse and J. Furthmüller, Phys. Rev. B **54**, 11169 (1996).
[6] G. Kresse and J. Furthmüller, Comput. Mater. Sci. **6**, 15 (1996).
[7] P. E. Blöchl, Phys. Rev. B **50**, 17953 (1994).
[8] G. Kresse and D. Joubert, Phys. Rev. B **59**, 1758 (1999).
[9] W. Setyawan and S. Curtarolo, Comp. Mater. Sci. **49**, 299 (2010).
[10] A. M. Ganose, A. J. Jackson, and D. O. Scanlon, J. Open Source Softw. **3**, 717 (2018).
[11] J. Luo, Z. Zhao, Y. Zhou, J. Yang, A. Fang, H. Yang, H. Gao, R. Zhou, and G.-q. Zheng, arXiv preprint arXiv:2108.10263 (2021).